



OPEN

SLM-processed MoS₂/Mo₂S₃ nanocomposite for energy conversion/storage applications

Navid Alinejadian^{1,2}, Sayed Habib Kazemi³ & Inger Odnevall^{4,5}✉

MoS₂-based nanocomposites have been widely processed by a variety of conventional and 3D printing techniques. In this study, selective laser melting (SLM) has for the first time successfully been employed to tune the crystallographic structure of bulk MoS₂ to a 2H/1T phase and to distribute Mo₂S₃ nanoparticles in-situ in MoS₂/Mo₂S₃ nanocomposites used in electrochemical energy conversion/storage systems (EECSS). The remarkable results promote further research on and elucidate the applicability of laser-based powder bed processing of 2D nanomaterials for a wide range of functional structures within, e.g., EECSS, aerospace, and possibly high-temperature solid-state EECSS even in space.

Na-S energy conversion/storage devices have earlier been demonstrated as possible alternatives to mitigate thermal decomposition, short circuit, heat, fire, or explosion of Li-ion electrodes^{1,2}. Recently has a high thermal stable hexagonal boron nitride (h-BN) been introduced as a promising anode material, though its low electrical conductivity may limit its electrochemical performance¹. Molybdenum disulfide (MoS₂) belongs to a class of advanced next-generation materials called Transition Metal Dichalcogenides (TMDs) with a direct bandgap of ~1.8 eV and a melting point of 1185 °C in nonoxidizing environments³. MoS₂, with strong covalent S–Mo–S bonds and weak inter-layer van der Waals forces⁴, and its nanocomposites dominate electroactive layered structures due to their transitional structure from semiconductor 2H to metallic 1T, which is favorable in electrochemical applications^{5,6}. Similar to Li⁺, the accommodation of Na⁺ between 1T-MoS₂ results in considerable capacitance and interesting electrochemical properties⁷.

MoS₂-based nanocomposites have been widely studied using a variety of conventional methods^{8–12} which have different technical drawbacks such as complex expensive pre-processing (exfoliation, preparation, and large-scale production), processing (deposition or lack of precise morphology control), and complementary post-processing stages (thermal, acid treatment, and limitation of geometric and specific surface area)^{6,13}. Despite the mitigation of existing drawbacks, scientists have enhanced processing possibilities which have led to novel 3D printing techniques^{14–20}. The use of these techniques is still limited due to drawbacks such as restricted resolution, weak mechanical properties, low printing speed, or high cost of equipment^{6,21–23}.

Laser-based thinning can effectively exfoliate MoS₂ in a controlled manner²⁴ to enable green fabrication of 3D shapes from 2D nanomaterials^{25,26}, and improve the charge capacitance properties of Mo₂S₃ nanostructures²⁷. The thinning mechanism of MoS₂, with a high laser absorption coefficient due to the weak van der Waals forces between poorly coupled MoS₂ layers, can be attributed to localized temperature-dependent sublimation of upper layers of bulk 2H-MoS₂ lattice, arising through the absorption of high-energy laser^{24,25,28}. At the next steps, laser irradiation on thinned 2H-MoS₂ can lead to further photoinduced exfoliation to form few-layered nanosheets²⁵. On the other hand, the more laser reflection due to the high reflection ratio of Mo powder²⁸, the more thinning of 2H-MoS₂ existing nearby Mo powders²⁵.

2H-MoS₂ is the thermodynamically stable trigonal phase consisting of prismatic coordination of Mo atoms by six surrounding sulfur atoms, whereas metallic 1T-MoS₂, metastable octahedral coordination of Mo atoms in MoS₂, can be a result of the first-order phase transition due to the change in the density of states²⁹. It has already been shown that the exfoliated form consists of a 1T-MoS₂ phase with lattice distortions according to

¹Department of Mechanical and Industrial Engineering, Tallinn University of Technology, 19086 Tallinn, Estonia. ²KTH Royal Institute of Technology, Division of Surface and Corrosion Science, Department of Chemistry, School of Engineering Sciences in Chemistry, Biotechnology and Health, Drottning Kristinas väg 51, 100-44 Stockholm, Sweden. ³Department of Chemistry, Institute for Advanced Studies in Basic Sciences, Zanjan 45137-66731, Iran. ⁴AIMES-Center for the Advancement of Integrated Medical and Engineering Sciences, Karolinska Institutet, KTH Royal Institute of Technology, Stockholm, Sweden. ⁵Department of Neuroscience, Karolinska Institutet, 171 77 Stockholm, Sweden. ✉email: ingero@kth.se

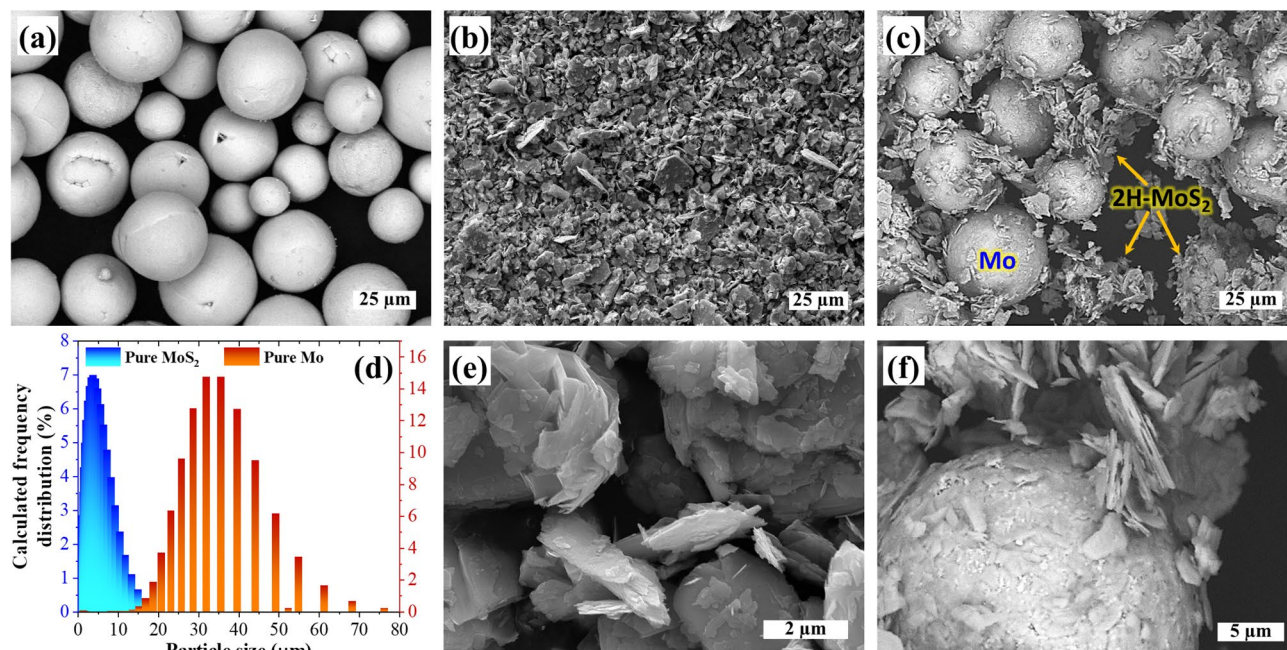


Figure 1. Scanning electron microscopy images of (a) pure Mo powder, (b) layered MoS₂ powder, and (c) Mo-MoS₂ powder mixture feedstock. (d) Particle size distribution plot of Mo and MoS₂ powders based on high-resolution scanning electron microscopy images of (e) layered MoS₂ powder and (f) the Mo-MoS₂ mixture feedstock.

the exfoliation technique. The annealing of metastable 1T-MoS₂ at temperatures lower than 300 °C can lead to restacking of the layers and restoration of 2H-MoS₂^{7,29,30}. Hence, generally, integrated hybrid 1T/2H-MoS₂ exists in which the 2H phase can stabilize the metastable 1T phase, avoiding restocking and restoration³⁰. It has though been proven that 2H-MoS₂ at temperatures higher than 600 °C can be transformed into 1T-MoS₂ via nucleation of an intermediate and subsequently 2H/1T boundaries migration over time³¹.

Accordingly, high-energy laser processing of MoS₂ can impose a highly localized temperature resulting in the thinning of MoS₂ as well as the creation of many α -phase nucleation sites for 2H to 1T phase transformation^{25,26,31}. Mo₂S₃ nanostructures can due to surface phase transformation also be formed through thermal annealing or sputtering of MoS₂ in an Ar-isolated atmosphere and at high temperatures above 1300 °C²⁵. Imposing sulfur vacancies into the structure of MoS₂ in the exposure of high-energy laser beam in the presence of melted Mo at a high temperature can also result in the formation of Mo₂S₃ nanostructures at the edges of laser-thinned 1T-MoS₂ and sulfur vacancies^{25,26}. Consequently, the rapid cooling rate of the SLM process as well as the presentation of Mo₂S₃ nanostructures can significantly prevent the restoration of 1T/2H-MoS₂.

Compared to other 3D printing methods, SLM relies on versatile high-energy Nd:YAG laser equipment which enables printing of parts of improved mechanical properties and better resolution. Since the SLM technique can overcome many of the demerits of both conventional and other 3D printing techniques^{6,21,23}, this technology can be used for rapid prototyping of future energy storage materials^{6,32}. Despite the specific characteristics of MoS₂ in electrochemical applications, the weak van der Waals forces make direct SLM processing of MoS₂ structures difficult. The addition of Mo powder, as a metallic additive, has been shown to both facilitate the printability of MoS₂ based structures and result in the formation of stable electrocatalytic Mo₂S₃ nanostructures via Mo-Mo zigzag chains, which enhance the electron transfer within and between the S-Mo-S layers²⁷.

This study reveals the extraordinary influence of the SLM technology not only on the crystallographic phase transformation of MoS₂ from bulk 2H to metallic 1T through one-step laser-based exfoliation but also on the simultaneous formation and uniform distribution of Mo₂S₃ nanoparticles in the nanocomposite structure. The unprecedented electroactivity of the one-step SLM-processed MoS₂/Mo₂S₃ nanocomposite (SLM-Mo_(s)S_(x+1)) is demonstrated, paving the way for the fabrication of the next generation EECSS. Our recent findings demonstrate that the SLM technique is able to directly utilize raw materials, exfoliate MoS₂ in-situ during fabrication of intricate parts, such as electroactive components of EECSS, and directly deliver parts of different functionalities without any special additives or binders.

Results

The spherical morphology of Mo and irregularly shaped MoS₂ particles can be ascertained from Fig. 1a,b,e, showing an average size (d_{50}) of 25–35 μ m and 2.5–7.5 μ m, respectively (Fig. 1d). Aside from slightly crushed pure MoS₂, its lamellar morphology was retained even after 6 h of mixing with pure Mo (Fig. 1c,f), enhancing the packing density³³ and the mean laser absorptivity^{25,28} of the Mo-MoS₂ mixture feedstock.

Illustrated in Fig. 6e (experimental), three types of defects were observed in the laser single scan (LSS) of powder bed; (i) lack of fusion (LOF) defects which were intensified by increased scan speed and reduced laser

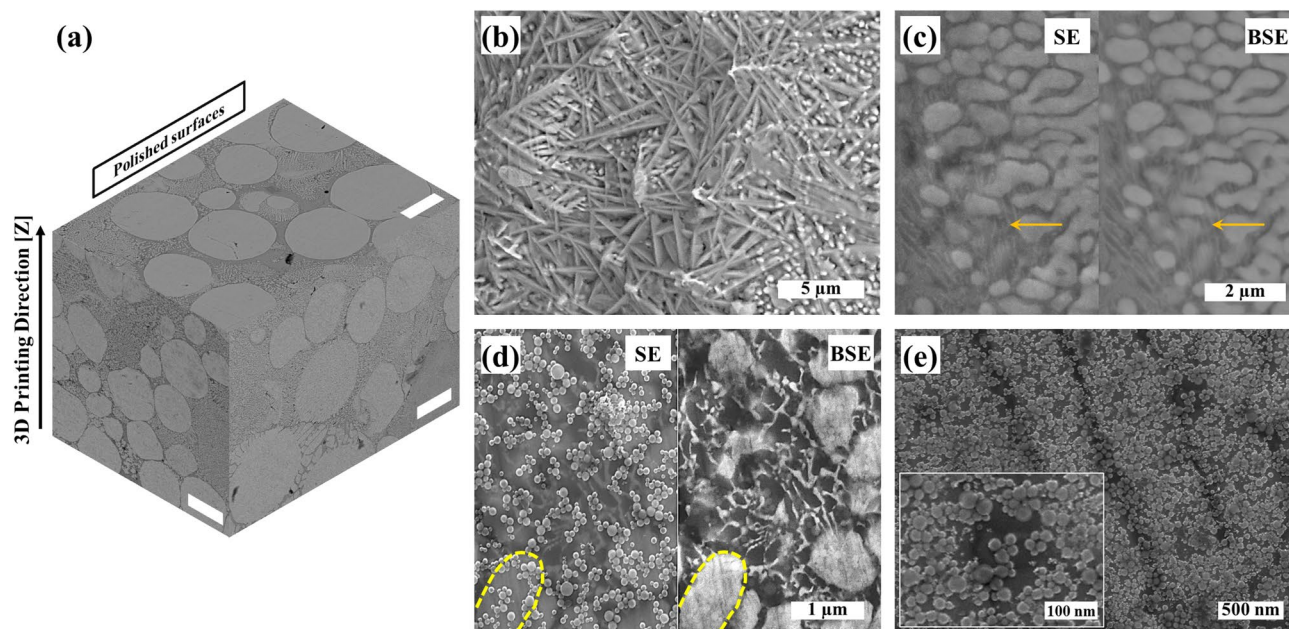


Figure 2. SEM micrographs of (a) polished surfaces of SLM- $\text{Mo}_{(x)}\text{S}_{(x+1)}$ (scale bar = 25 μm), (b) unpolished top-surface including laser-assisted exfoliated 1T- MoS_2 nanosheets and Mo_2S_3 nanoparticles, (c) high magnification secondary and backscattered electron micrographs acquired from the polished cross-section in which the arrows indicate thin transparent 1T- MoS_2 layers alongside coalesced Mo_2S_3 nanoparticles, (d) HR-SEM micrograph of the polished surface of SLM- $\text{Mo}_{(x)}\text{S}_{(x+1)}$ in which the yellow dashed lines indicate coalescence zones of Mo_2S_3 nanoparticles, and (e) high magnification HR-SEM micrograph of a cross-section showing Mo_2S_3 nanoparticles within the structure of the nanocomposite.

power, (ii) balling defects due to the insufficient imposed energy density either at high scan speeds or low laser powers, and (iii) over melting of the powder bed at high energy densities due to both high laser power and low scan speed²⁸. The 3D SEM micrograph from different polished sections of SLM- $\text{Mo}_{(x)}\text{S}_{(x+1)}$ indicated a similar microstructure which can be ascribed to the optimized LSS (laser power of 62.5 W and a laser scan speed of 85 mm s^{-1}) resulting in a relatively stable melt-pool with a nearly constant thermal gradient during the SLM process (Fig. 2a)^{34,35}. Scanning electron micrographs (SEM) illustrate the exfoliation of bulk 2H- MoS_2 into thin 1T- MoS_2 nanosheets and the distribution of Mo_2S_3 nanoparticles in the matrix (Fig. 2b). Both the back-scattered (BSE) and the secondary-electron (SE) micrographs elucidate the presence of 1T- MoS_2 layers of low density (Fig. 2c,d). Indicating identical zones, the arrows in Fig. 2c and the dashed lines in Fig. 2d, confirm the presence of Mo_2S_3 nanoparticles coalesced at the lower parts- and separated at the top surface of the nanocomposite, delimited by a transparent 1T- MoS_2 layer. The coalescence is attributed to partial remelting of the subsequent layers during the layer-wise SLM process. HR-SEM micrographs (Fig. 2e) reveal a uniform distribution of Mo_2S_3 nanoparticles sized between 25 and 50 nm. The spherical particle morphology is attributed to the high surface tension between MoS_2 and Mo_2S_3 due to varying Mo/S ratios and the tendency of resolidified nanostructures to reduce their surface energies²⁵.

The X-ray diffraction (XRD) patterns verified the purity of Mo and MoS_2 both before and after the mixing process (Fig. 3a). The low-intensity XRD peaks confirm the presence of Mo_2S_3 along with pure 1T/2H- MoS_2 crystallographic planes (Fig. 3b). Both the exfoliation and the phase transformation of 2H- MoS_2 resulted in diffraction peaks related to the 001 plane of 1T- MoS_2 ($2\theta = 10.495^\circ$)⁷. Illustrated in Fig. 3c, the broadening and blue shift of the E_{2g}^1 and A_{1g} Raman peaks from 384 cm^{-1} (E_{2g}^1) and 409 cm^{-1} to 380 cm^{-1} and 406 cm^{-1} , respectively, confirm the Nd:YAG laser-assisted thinning and transformation of 2H- MoS_2 to a few-layered 1T- MoS_2 at the temperature elevated above 650° K^{25,26}. Besides, the existence of Mo_2S_3 nanoparticles was verified by the appearance of two shoulders associated with E_{2g}^1 and A_{1g} Raman peaks of Mo_2S_3 at 376 cm^{-1} and 403 cm^{-1} , respectively²⁵.

Cyclic voltammograms (CV) show considerably enhanced current densities for the SLM- $\text{Mo}_{(x)}\text{S}_{(x+1)}$ sample compared to both pure Mo and MoS_2 electrodes (Fig. 4a). Due to the presence of the Mo_2S_3 nanoparticles as well as the laser-based thinning and crystallographic phase transformation of MoS_2 from 2H to 1T, it is evident that the CV loops retained their nearly rectangular shapes even at high scan rates (100 mV s^{-1}) (Fig. 4b)⁷. Quasi-symmetrical triangle plots of the galvanostatic charge–discharge (GCD) at different current densities revealed nearly 1.0 V in output voltage even at a current density of 15 mA cm^{-2} for the SLM- $\text{Mo}_{(x)}\text{S}_{(x+1)}$ electrodes (Fig. 4c). Herein, we observed considerable capacitance enhancement up to 2000 cycles of GCD at a current density of 8 mA cm^{-2} . This confirms an increased areal capacitance (from 41 to 121.2 mF cm^{-2}) and a decreased iR voltage drop. The enhanced capacitance induced by increasing the number of GCD cycles can be attributed to facilitated intercalation of Na^+ cations, activation of the electrode texture, and improved electrical conductivity (Fig. 4d). It can also be ascribed to the penetration of electrolyte into micro-holes of the structure,

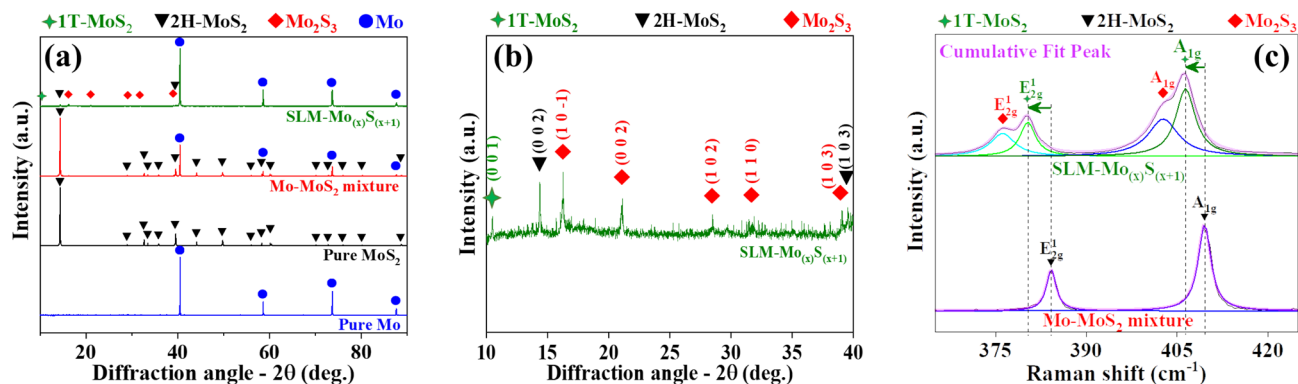


Figure 3. (a) XRD patterns of the pure Mo powder, MoS₂ powder, Mo-MoS₂ powder mixture, and SLM-Mo_(x)S_(x+1) samples, (b) magnified XRD peaks between $10 \leq 2\theta \leq 40$ showing the presence of 1T-MoS₂, 2H-MoS₂, and Mo₂S₃ phases in the nanocomposite and (c) Raman spectra with the deconvoluted profiles of 1T-MoS₂, 2H-MoS₂, and Mo₂S₃ nanoparticles showing the shift in their position.

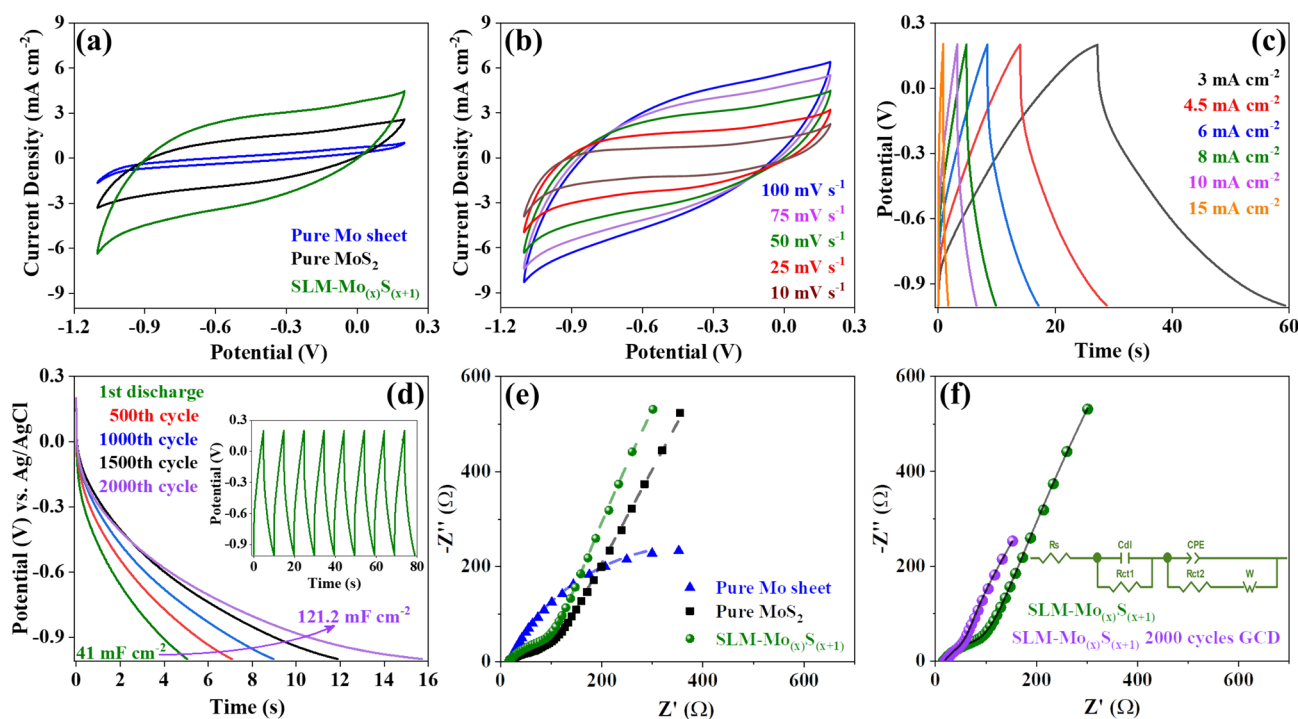


Figure 4. Electrochemical characterization in a 0.5 M Na₂SO₄: (a) CV curves of pure Mo sheet, pure MoS₂, and SLM-Mo_(x)S_(x+1) by using a scan rate of 50 mV s⁻¹, (b) cyclic voltammograms for different scan rates from 10 to 100 mV s⁻¹, (c) GCD curves for different current densities from 3 to 15 mA cm⁻², (d) discharge retention stability after 500, 1000, 1500, and 2000 cycles of GCD at a current density of 8 mA cm⁻², and (e) Nyquist plot of pure Mo sheet, pure MoS₂, and SLM-Mo_(x)S_(x+1) in the frequency range between 10⁻¹ Hz to 100 kHz, (f) Nyquist plot of SLM-Mo_(x)S_(x+1) in the frequency range between 10⁻¹ Hz to 100 kHz before and after 2000 cycles of GCD at a current density of 8 mA cm⁻².

successively activating deeper electro-active sites, and possibly a continued activation of sub-layers beneath the SLM-Mo_(x)S_(x+1) surface^{36,37}.

As shown in Fig. 4e, faster kinetic of the charge transfer at the interface offered by the layered 1T-MoS₂, separated by Mo₂S₃ nanoparticles, resulted in a considerably lower R_{ct} (75.36 Ω) and a quasi-semicircle shape of the Nyquist plot of SLM-Mo_(x)S_(x+1) compared to pure Mo. The higher slope of the diffusion impedance in the low-frequency region for SLM-Mo_(x)S_(x+1) compared to pure 2H-MoS₂, confirms facilitated diffusion and accumulation of Na⁺ charges into the defect-rich 1T-MoS₂ nanolayers within the porous surface (Fig. 4e)³⁸. Comparing the SLM-Mo_(x)S_(x+1) electrode before and after 2000 cycles GCD in Fig. 4f, showed a considerably decreased diameter of the quasi-semicircle of the Nyquist plot (charge transfer resistance) at high frequencies as well as an increased slope of the diffusion impedance in the low-frequency region. This further verify faster

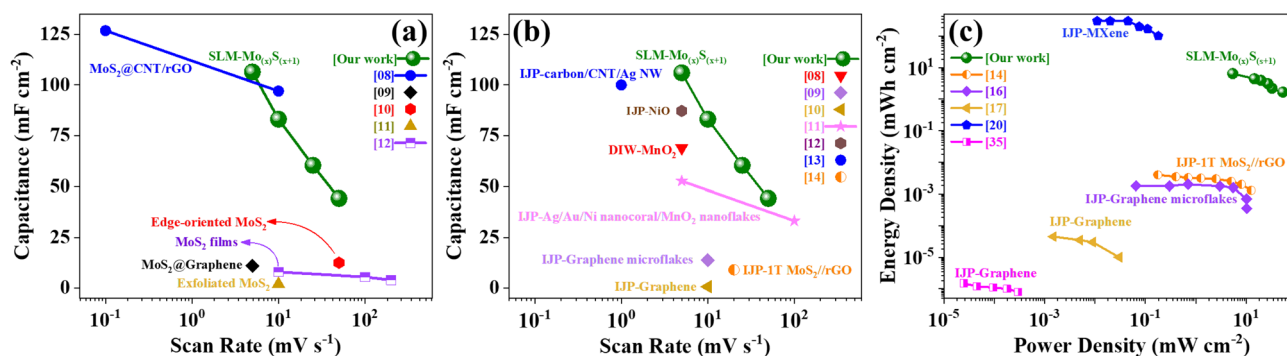


Figure 5. (a) Areal rate capacitance for different MoS₂-based structures processed by various conventional methods for energy storage devices (the weight percentage in parenthesis indicates the amount of MoS₂ in the structure); (b) areal rate capacitance for different materials processed with various 3D printing methods for energy storage applications and (c) Ragone plot comparing the areal power density versus areal energy density of 3D-printed electrodes intended for energy storage applications.

kinetics of the interface charge transfer and facilitated Na⁺ intercalation into the deeper active sites and spaces of electrode materials, respectively, by increasing the number of GCD cycles.

Areal rate capability studies of the SLM-Mo_(x)S_(1+x) electrode revealed capacitance retention of 53% even at a scan rate of 50 mV s⁻¹ (44.16 mF cm⁻²) compared to a low scan rate of 10 mV s⁻¹ (83.1 mF cm⁻²). This is considerably higher than their counterpart electrodes processed by different 3D printing techniques (Fig. 5a,b). Furthermore, according to the Ragone plot (Fig. 5c), the SLM-Mo_(x)S_(1+x) electrodes offered higher power (53.34 mW cm⁻²) and energy density (1.66 mWh cm⁻²) compared with ink-jet printed MXene³⁹, and graphene-based electrodes^{16,17,40}, as well as 1T-MoS₂/graphene-based electrodes¹⁴.

Concluding remarks

The successful fabrication of SLM-processed MoS₂/Mo₂S₃ electrodes with a remarkable capacitive behavior compared to other 3D-printed counterparts provides a new possibility to manufacture the next generation of 3D-printed electrochemical devices. In this study, we elucidate that a high-energy Nd:YAG laser can simultaneously exfoliate and tune the structure of MoS₂, distribute electroactive Mo₂S₃ nanoparticles into the structure of the nanocomposite, and therefore considerably enhance the power density and energy density of 3D-printed structures. The preliminary results promote further research on laser-based processing of 2D nanomaterials for a wide range of functional structures e.g., EECSS, high-temperature solid-state energy conversion/storage systems, aerospace parts, and green energy storage device fabrication, even in space.

Materials and methods

Gas atomized powder (GAP) of commercial pure molybdenum (Mo, 99.99%) was used as the feedstock to fabricate both the current collector and the electroactive nanocomposite. Pure molybdenum disulfide powder (2H-MoS₂, 99.99%, Sigma Aldrich) was used as feedstock for SLM processing of the electroactive nanocomposite. A mixture of Mo and MoS₂ (20 wt.%) was prepared by mixing for 6 h at 20 rpm to obtain a homogenous mixture (Fig. 6a,d). The Na₂SO₄ (≥99.0%, Merck) and ultrapure water, with a conductivity of 18.2 MΩcm and a pH of 6.5 ± 0.1 at 25 °C, was used to prepare the 0.5 M Na₂SO₄ (pH 5.5 ± 0.1) electrolyte for the electrochemical investigations.

A laser scattering particle size distribution analyzer (LPSA, LA-950, HORIBA, Japan) was used to evaluate the particle size distribution of the Mo and MoS₂ powders. A Realizer GmbH SLM-50 device equipped with Nd:YAG laser was used for SLM processing of pure Mo as a substrate/current collector and MoS₂/Mo₂S₃ nanocomposite as the electroactive structure. The 316L substrate platform was used to fabricate the samples at ambient conditions. Laser single scanning (LSS) was carried out as a function of energy density to obtain the optimized printing parameters, where the energy density is defined in Eq. (1):

$$E_d = P/(v \cdot h \cdot t) \quad (1)$$

where P is the laser power, v is the laser scan speed, h is the hatch distance, and t is the layer thickness. The hatch distance and layer thickness were kept constant at 0.045 mm and 0.025 mm, respectively. The schematic of single laser scanning on a powder bed to form a single hatch has been illustrated in Fig. 6b. commensurately shown in Fig. 6e, the laser power and scan speed were varied between 25 and 75 W and 65–550 mm s⁻¹, respectively. The disk-shaped electrodes were fabricated of a mixture of Mo and MoS₂ (20 wt.%) by using optimized SLM parameters (laser power – 62.5 W and scan speed – 85 mm s⁻¹). Figure 6c illustrates the continued scanning of powder-bed leading to consolidation and formation of one layer onto the previously printed and solidified sub-layers (Supplementary Information). Each layer can contain approximately 14 mg MoS₂. Shown in Fig. 6f, both the sintered particles in the boundary between melted/solidified region (red arrow) and un-melted powder bed (yellow arrow) and overlapping of hatches (vertical lines indicated by the blue arrow) are evident. Hatch size (a) and hatch overlap ($a - \Delta x$) have been illustrated in Fig. 6b,c, respectively.

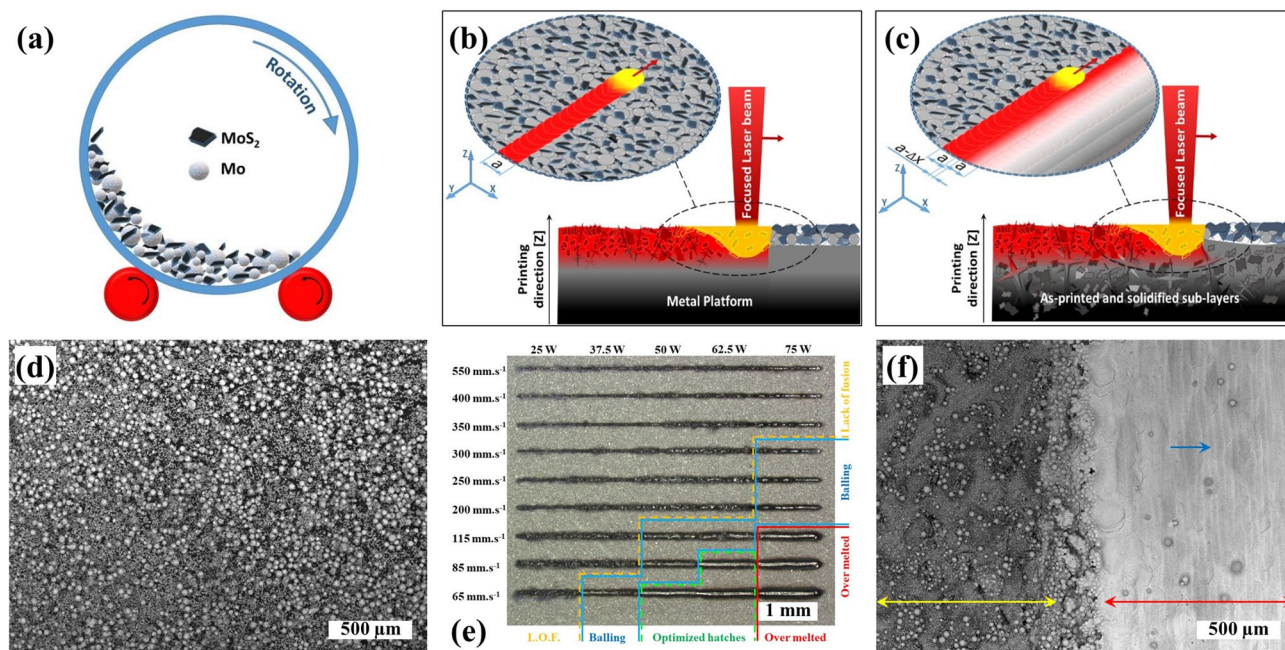


Figure 6. Schematic illustrating the (a) mixing of Mo and MoS₂ powders, (b) single laser scanning, and (c) laser-based fusion of the powder bed with partial remelting of the previously solidified layer. (d) SEM images of a homogenous mixture of Mo and MoS₂ powders, (e) stereomicrograph of laser single scan as a function of energy density, and (f) SEM image of the half-melted sample showing the boundary between the melted/solidified (red arrow), un-melted powder bed (yellow arrow), and hatch overlap during continues single laser scanning of powder bed (blue arrow).

A stereomicroscope (V20, Zeiss, Germany) was used to study the effect of different single laser scanning parameters on the stability of the melt pool to optimize the 3D printing parameters (Fig. 6e). An ultrasonic bath (USC300TH, VWR, Malaysia) was used to prepare and degas the 0.5 M Na₂SO₄ electrolyte as well as to clean the surface of the 3D-printed electrodes. A standard pH meter (PHM210, Radiometer Analytical-Hack, France) was used to measure the pH of the Na₂SO₄ electrolyte. A PARSTAT MC multichannel potentiostat (AMETEK, Princeton Applied Research, USA), an Ag/AgCl reference electrode (AMETEK, Princeton Applied Research, USA), and a Pt wire counter electrode (CHI115, CH Instruments Inc., USA) were used for the electrochemical studies. The surface area of the working electrode (anode) was 0.33 cm². Cyclic voltammetry (CV) was carried out using scan rates between 10 and 100 mV s⁻¹ in a potential window between -1.1 and 0.2 V. Electrochemical potentiostatic impedance (EIS) measurements were carried out in the frequency range between 10⁻¹ Hz and 100 kHz (Figure S4b). Galvanostatic charge–discharge (GCD) measurements were carried out at different current densities (3, 4.5, 6, 8, 10, and 15 mA cm⁻²). 2000 cycles of GCD at a current density of 8 mA cm⁻² were performed on the electrodes to evaluate their stability and capacity retention.

X-ray diffraction (XRD) studies were carried out by using a Smartlab (Rigaku, Japan) diffractometer equipped with a rotating 9 kW Cu anode X-ray tube with Cu-Kα1 radiation ($\lambda = 1.5406 \text{ \AA}$), and a silicon strip detector D/teX Ultra. Based on the Rigaku database, ICDD card numbers 9008543, 1531960, and 1531960 were selected to identify the XRD patterns of Mo, MoS₂, and Mo₂S₃, respectively. Raman measurements were carried out using a Horiba LabRAM HR800 micro-Raman system equipped with a cooled multichannel CCD detection system in the back-scattering configuration with a spectral resolution of 1 cm⁻¹. A Nd:YAG laser ($\lambda = 532 \text{ nm}$) was used for excitation with a laser spot size diameter of approximately 5 μm. A high-resolution scanning electron microscope (HR-SEM, Zeiss MERLIN, Germany) was employed to study the surface morphology of 3D-printed samples in both back-scattered (BE) and secondary (SE) electron modes (Supplementary Information).

Data availability

All data generated or analyzed during this study are included in this published article, and the datasets used and analyzed during the current study are available from the corresponding author on reasonable request.

Received: 2 February 2022; Accepted: 15 March 2022

Published online: 23 March 2022

References

- Mussa, Y., Ahmed, F., Arsalan, M. & Alsharaeh, E. Two dimensional (2D) reduced graphene oxide (RGO)/hexagonal boron nitride (h-BN) based nanocomposites as anodes for high temperature rechargeable lithium-ion batteries. *Sci. Rep.* **10**, 1–13 (2020).
- Yoo, H. D., Markevich, E., Salitra, G., Sharon, D. & Aurbach, D. On the challenge of developing advanced technologies for electrochemical energy storage and conversion. *Mater. Today* **17**, 110–121 (2014).

3. Chhowalla, M. *et al.* The chemistry of two-dimensional layered transition metal dichalcogenide nanosheets. *Nat. Chem.* **5**, 263–275 (2013).
4. Lu, J., Liu, H., Tok, E. S. & Sow, C.-H.H. Interactions between lasers and two-dimensional transition metal dichalcogenides. *Chem. Soc. Rev.* **45**, 2494–2515 (2016).
5. Fleischmann, S. *et al.* Pseudocapacitance: From fundamental understanding to high power energy storage materials. *Chem. Rev.* **120**, 6738–6782 (2020).
6. Alinejadian, N., Kollo, L. & Odnevall, I. Materials science in semiconductor processing progress in additive manufacturing of MoS₂-based structures for energy storage applications—A review. *Mater. Sci. Semicond. Process.* **139**, 106331 (2022).
7. Acerce, M., Voiry, D. & Chhowalla, M. Metallic 1T phase MoS₂ nanosheets as supercapacitor electrode materials. *Nat. Nanotechnol.* **10**, 313–318 (2015).
8. Wang, S. *et al.* Three-dimensional MoS₂@CNT/RGO network composites for high-performance flexible supercapacitors. *Chem. A Eur. J.* **23**, 3438–3446 (2017).
9. Bissett, M. A., Kinloch, I. A. & Dryfe, R. A. W. Characterization of MoS₂-graphene composites for high-performance coin cell supercapacitors. *ACS Appl. Mater. Interfaces* **7**, 17388–17398 (2015).
10. Yang, Y., Fei, H., Ruan, G., Xiang, C. & Tour, J. M. Edge-oriented MoS₂ nanoporous films as flexible electrodes for hydrogen evolution reactions and supercapacitor devices. *Adv. Mater.* **26**, 8163–8168 (2014).
11. Winchester, A. *et al.* Electrochemical characterization of liquid phase exfoliated two-dimensional layers of molybdenum disulfide. *ACS Appl. Mater. Interfaces* **6**, 2125–2130 (2014).
12. Cao, L. *et al.* Direct laser-patterned micro-supercapacitors from paintable MoS₂ films. *Small* **9**, 2905–2910 (2013).
13. Lin, Z. *et al.* Solution-processable 2D semiconductors for high-performance large-area electronics. *Nature* **562**, 254–258 (2018).
14. Shao, Y. *et al.* 3D crumpled ultrathin 1T MoS₂ for inkjet printing of Mg-ion asymmetric micro-supercapacitors. *ACS Nano* **14**, 7308–7318 (2020).
15. Wang, T. *et al.* 3D printing-based cellular microelectrodes for high-performance asymmetric quasi-solid-state micro-pseudocapacitors. *J. Mater. Chem. A* **8**, 1749–1756 (2020).
16. Sollami Delekta, S., Laurila, M.-M., Mäntysalo, M. & Li, J. Drying-mediated self-assembly of graphene for inkjet printing of high-rate micro-supercapacitors. *Nano-Micro Lett.* **12**, 40 (2020).
17. Li, J. *et al.* Scalable fabrication and integration of graphene microsupercapacitors through full inkjet printing. *ACS Nano* **11**, 8249–8256 (2017).
18. Lin, Y., Gao, Y. & Fan, Z. Printable fabrication of nanocoral-structured electrodes for high-performance flexible and planar supercapacitor with artistic design. *Adv. Mater.* **29**, 1–8 (2017).
19. Giannakou, P., Tas, M. O., Le Borgne, B. & Shkunov, M. Water-transferred, inkjet-printed supercapacitors toward conformal and epidermal energy storage. *ACS Appl. Mater. Interfaces* **12**, 8456–8465 (2020).
20. Choi, K. H., Yoo, J. T., Lee, C. K. & Lee, S. Y. All-inkjet-printed, solid-state flexible supercapacitors on paper. *Energy Environ. Sci.* **9**, 2812–2821 (2016).
21. Cheng, M., Deivanayagam, R. & Shahbazian-Yassar, R. 3D printing of electrochemical energy storage devices: A review of printing techniques and electrode/electrolyte architectures. *Batter. Supercaps* **3**, 130–146 (2020).
22. Egorov, V. *et al.* Evolution of 3D printing methods and materials for electrochemical energy storage. *Adv. Mater.* **32**, 1–27 (2020).
23. Zhang, F. *et al.* 3D printing technologies for electrochemical energy storage. *Nano Energy* **40**, 418–431 (2017).
24. Castellanos-Gomez, A. *et al.* Laser-thinning of MoS₂: On demand generation of a single-layer semiconductor. *Nano Lett.* **12**, 3187–3192 (2012).
25. Alexaki, K., Kostopoulou, A., Sygletou, M., Kenanakis, G. & Stratakis, E. Unveiling the structure of MoS₂ nanocrystals produced upon laser fragmentation of MoS₂ platelets. *ACS Omega* **3**, 16728–16734 (2018).
26. Hu, L., Shan, X., Wu, Y., Zhao, J. & Lu, X. Laser thinning and patterning of MoS₂ with layer-by-layer precision. *Sci. Rep.* **7**, 1–9 (2017).
27. Zhou, X. *et al.* Urchin-like Mo₂S₃ prepared via a molten salt assisted method for efficient hydrogen evolution. *Chem. Commun.* **54**, 12714–12717 (2018).
28. Wang, D., Yu, C., Ma, J., Liu, W. & Shen, Z. Densification and crack suppression in selective laser melting of pure molybdenum. *Mater. Des.* **129**, 44–52 (2017).
29. Eda, G. *et al.* Photoluminescence from chemically exfoliated MoS₂. *Nano Lett.* **11**, 5111–5116 (2011).
30. Wang, D. *et al.* Phase engineering of a multiphase 1T/2H MoS₂ catalyst for highly efficient hydrogen evolution. *J. Mater. Chem. A* **5**, 2681–2688 (2017).
31. Lin, Y. C., Dumcenco, D. O., Huang, Y. S. & Suenaga, K. Atomic mechanism of the semiconducting-to-metallic phase transition in single-layered MoS₂. *Nat. Nanotechnol.* **9**, 391–396 (2014).
32. Zhu, C. *et al.* 3D printed functional nanomaterials for electrochemical energy storage. *Nano Today* **15**, 107–120 (2017).
33. Körner, C., Attar, E. & Heinel, P. Mesoscopic simulation of selective beam melting processes. *J. Mater. Process. Technol.* **211**, 978–987 (2011).
34. Yuan, W., Chen, H., Cheng, T. & Wei, Q. Effects of laser scanning speeds on different states of the molten pool during selective laser melting: Simulation and experiment. *Mater. Des.* **189**, 108542 (2020).
35. Leitz, K. H. *et al.* Multi-physical simulation of selective laser melting. *Met. Powder Rep.* **72**, 331–338 (2017).
36. Kazemi, S. H., Hosseinzadeh, B., Kazemi, H., Kiani, M. A. & Hajati, S. Facile synthesis of mixed metal-organic frameworks: Electrode materials for supercapacitors with excellent areal capacitance and operational stability. *ACS Appl. Mater. Interfaces* **10**, 23063–23073 (2018).
37. Bahmani, F. *et al.* CuMnO₂-reduced graphene oxide nanocomposite as a free-standing electrode for high-performance supercapacitors. *Chem. Eng. J.* **375**, 121966 (2019).
38. Li, Y. *et al.* Hierarchical MoS₂ hollow architectures with abundant Mo vacancies for efficient sodium storage. *ACS Nano* **13**, 5533–5540 (2019).
39. Zhang, C. *et al.* Additive-free MXene inks and direct printing of micro-supercapacitors. *Nat. Commun.* **10**, 1–9 (2019).
40. Li, L. *et al.* High-performance solid-state supercapacitors and microsupercapacitors derived from printable graphene inks. *Adv. Energy Mater.* **6**, 1600909 (2016).

Acknowledgements

Dr. Lauri Kollo, Prof. Maarja Grossberg, and Dr. Olga Volobujeva, are acknowledged for their research support and technical discussion. Dr. Xuying Wang is acknowledged for providing electrodes and tools. Prof. Prashanth KondaGokuldoss is acknowledged for sharing his initial opinions and providing powder feedstock. Dr. Pei Wang is appreciated for providing pure Mo powder. The research was funded by the European Regional Development Fund [ASTRA6-6], the Estonian Education and Youth Board and the Estonian Government [contract number: 5.10-6.1/21/23-4 and 5.10-6.1/21/327-2].

Author contributions

N.A.: conceptualization; SLM processing, experiments, and characterizations by SEM, XRD, Raman spectroscopy, and all electrochemical characterization; funding acquisition; investigation; writing original draft, reviewing, editing, and validation of data. S.H.K.: advisory of electrochemical characterizations; formal analysis, review, editing, and validation of data. I.O.: supervision, providing resources, instrumentation, and analytical tools, formal analysis, reviewing, editing, and validation of data.

Funding

Open access funding provided by Royal Institute of Technology.

Competing interests

The authors declare no competing interests.

Additional information

Supplementary Information The online version contains supplementary material available at <https://doi.org/10.1038/s41598-022-08921-7>.

Correspondence and requests for materials should be addressed to I.O.

Reprints and permissions information is available at www.nature.com/reprints.

Publisher's note Springer Nature remains neutral with regard to jurisdictional claims in published maps and institutional affiliations.



Open Access This article is licensed under a Creative Commons Attribution 4.0 International License, which permits use, sharing, adaptation, distribution and reproduction in any medium or format, as long as you give appropriate credit to the original author(s) and the source, provide a link to the Creative Commons licence, and indicate if changes were made. The images or other third party material in this article are included in the article's Creative Commons licence, unless indicated otherwise in a credit line to the material. If material is not included in the article's Creative Commons licence and your intended use is not permitted by statutory regulation or exceeds the permitted use, you will need to obtain permission directly from the copyright holder. To view a copy of this licence, visit <http://creativecommons.org/licenses/by/4.0/>.

© The Author(s) 2022